scientific reports



OPEN

Preparation of efficient and reusable lanthanum and iron co-modified soda residue for selective phosphate removal from domestic sewage

Huiteng Wang¹, Hui Luo^{1,2⊠}, Rubin Han¹, Wenbo Wu¹, Jing Yang¹, Teng Qin¹, Limin Chen¹, Meng Liu¹, Bao-Jie He^{3,4,5} & Zhaoqian Jing⁶

The selection of suitable raw materials as adsorbents is a key factor in effectively removing phosphorus from water. As an industrial by-product, soda residue exhibits high porosity and surface area, which can effectively adsorb pollutants. Magnetic lanthanum-iron soda residue (La-Fe-CSR) was synthesized using the co-precipitation method, and its characterization and mechanism for removing phosphate were thoroughly investigated. La-Fe-CSR exhibited good adsorption performance under acidic conditions (3 < pH < 7). A high concentration of HCO_3^- (100 mg/L) reduced the adsorption performance of La-Fe-CSR by $8.3\% \pm 2.5\%$, whereas the presence of other coexisting ions had a smaller impact. The adsorption of phosphate by La-Fe-CSR was controlled by chemisorption and reached saturation after approximately 120 min. The phosphate adsorption by La-Fe-CSR was significantly higher than that of soda residue ($43.65 \pm 3.39 \text{ mg/g}$), reaching $74.87 \pm 2.46 \text{ mg/g}$. Ligand exchange and inner-sphere complexation constituted the primary mechanisms through which L-Fe-CSR removed phosphate. After 5 consecutive cycles, La-Fe-CSR maintained a phosphate removal efficiency of $74.5 \pm 1.6\%$. It demonstrated good performance in removing total phosphorus from real domestic sewage, with a removal rate of $94.9 \pm 0.5\%$. These research findings demonstrated that La-Fe-CSR held significant promise as a highly effective phosphate adsorbent in practical applications.

Keywords Soda residue, Calcination, Lanthanum, Phosphate adsorption, Magnetization, Domestic sewage

Phosphorus, an essential nutrient in ecosystems, facilitates the growth of plants and microorganisms¹. However, excessive phosphorus inputs have emerged as a predominant cause of eutrophication in global freshwater systems². Eutrophication disrupts biodiversity and ecological balance in aquatic environments, resulting in ecological issues like dissolved oxygen depletion and harmful algal blooms, which threaten water resource sustainability and ecological health³. To control eutrophication in freshwater systems, reducing external phosphorus sources (EPS) is important⁴. Previous studies have shown that the total phosphorus concentration in runoff entering lakes and other enclosed water bodies should not exceed 0.05 mg/L⁵. EPS mainly consists of domestic sewage, agricultural activities, and industrial wastewater⁶.

Recently, there has been increasing attention on using natural materials and industrial by-products as adsorbents to control EPS, including phosphogypsum⁷, soda residue (SR)⁸, clay⁹ and red mud¹⁰. SR, a potent alkaline waste produced in industrial manufacturing, not only occupies significant land resources but also causes land salinization, posing substantial pollution to the ecological environment¹¹. Consequently, the resource utilization of SR has emerged as a pressing issue. Previous studies have demonstrated that SR effectively removes heavy metals and organic pollutants from wastewater, and can also be utilized for flue gas desulfurization and

¹School of Civil and Ocean Engineering, Jiangsu Ocean University, Lianyungang 222005, China. ²Institute of Oceanology, Chinese Academy of Sciences, Qingdao 266071, China. ³Centre for Climate-Resilient and Low-Carbon Cities, School of Architecture and Urban Planning, Chongqing University, Chongqing 400030, China. ⁴Key Laboratory of New Technology for Construction of Cities in Mountain Area, Ministry of Education, Chongqing University, Chongqing 400044, China. ⁵Network for Education and Research On Peace and Sustainability (NERPS), Hiroshima University, Hiroshima 739-8530, Japan. ⁶College of Civil Engineering, Nanjing Forestry University, Nanjing 210037, China. [⊠]email: water@njfu.edu.cn

soil remediation¹². However, fewer studies have focused on SR as an adsorbent for controlling EPS. Currently, studies investigating the phosphorus removal performance of SR primarily involve alkali modification¹³, SR-based geopolymer¹⁴, calcination¹⁵, and SR-modified straw biochar⁸. These modification methods have to some extent improved SR adsorption capacity for phosphorus. However, these modified SR adsorbents are all non-magnetic, meaning that it is difficult to recover them after adsorbing phosphorus. This not only increases the risk of phosphorus release into the water, but these modified SRs may also produce alkaline sludge during phosphorus removal, which can further pollute the water body¹². Therefore, it is crucial to find a feasible method to utilize SR effectively.

Recent studies have found that the drawbacks of non-magnetic sorbents can be addressed by employing magnetic sorbents¹⁶. Adsorption-saturated magnetic adsorbents can be recovered and reused through magnetic methods, a process that not only enhances resource utilization efficiency but also offers significant economic benefits¹⁷. However, magnetic adsorbents continue to encounter challenges, with the possibility of adsorbed phosphorus being released back into the water under varying environmental conditions, such as in anoxic environments¹⁸. Lanthanum-based adsorbents are highly effective in removing phosphorus from water because lanthanum (La) can form stable precipitates with phosphorus¹⁹. It has been shown that incorporating La into magnetic adsorbents can further enhance their phosphorus removal capabilities, with adsorbed phosphorus being less susceptible to release back into the water column amidst environmental changes²⁰.

Based on this, the present study envisioned developing a new magnetic lanthanum-based adsorbent from the industrial by-product SR. Previous studies have shown that following calcination, SR displays a porous structure and an increased specific surface area¹⁵, which are beneficial for impregnating active binding sites. Therefore, we calcined the SR first and then loaded Fe and La through co-precipitation to obtain magnetic lanthanum-based calcined SR (La-Fe-CSR). The study aimed to achieve the following objectives: (1) to synthesize La-Fe-CSR for removal phosphate from domestic sewage; (2) to investigate how initial solution pH and co-existing ions impact phosphate adsorption; (3) to determine adsorption kinetics and isotherm parameters; (4) to explore the mechanisms of phosphate adsorption; (5) to investigate the recoverable and regenerative properties as well as the ability to remove phosphate in real domestic sewage. This research sought to evaluate the potential of magnetic La-modified SR as an adsorbent for mitigating eutrophication risks in water bodies and to provide guidance for the rational utilization of SR.

Materials and methods Materials and chemical

The SR was sourced from Lianyungang Alkali Industry Co., Ltd., China. In our previous study, we showed that SR mainly consists of $CaCO_3$, $CaSO_4$, and small amounts of Mg salts, with particle sizes typically ranging from 0.01 mm to 0.07 mm²¹. Before use, SR was washed with deionized water, dried in an oven (105 °C), ground, and passed through a 0.15 mm sieve. A specific amount of the treated SR was then calcined at 800 °C for 2 h. Finally, calcined SR was obtained and recorded as CSR.

FeCl $_3$ ·6H $_2$ O (99%), FeSO $_4$ ·7H $_2$ O (99%), KH $_2$ PO $_4$ (99.5%), La(NO $_3$) $_3$ ·6H $_2$ O (99.9%), HCl (36.0–38.0%), NaCl (\geq 99.5%), NaOH (\geq 98%), Na $_2$ NO $_3$ (99%), MgCl $_2$ (\geq 98.0%), NaHCO $_3$ (\geq 99.5%), CaCl $_2$ (\geq 96.0%) and Na $_2$ SO $_4$ (\geq 99.0%)were purchased from Shanghai National Pharmaceuticals Chemical Reagent Co., Ltd. (China). All chemical reagents used were of analytical purity, and the experimental solutions were prepared with deionized water.

Material preparation

Fe-CSR and La-Fe-CSR were synthesized using a co-precipitation method according to the previously reported method with minor adjustments ¹⁶, and the preparation flowchart is depicted in Fig. 1. Initially, a 50 mL solution of CaCl₂ (1 mol/L) was prepared, in which 5 g of CSR was added and shaken for 24 h (298 K, 150 r/min). Next, the suspension was moved to a conical flask using deionized water (50 mL). Then, 50 mL of ferric chloride hexahydrate solution (0.43 mol/L) and 50 mL of ferrous sulfate heptahydrate solution (0.215 mol/L) were added. Stirred the solution with a constant-temperature magnetic stirrer until the temperature reached 343 K. Subsequently, the pH was adjusted to 10.5 with NaOH (1 mol/L), and the solution was allowed to stabilize for 1 h. Finally, the resulting product was collected from the suspension via magnetic separation, washed with deionized water, milled, and dried to obtain Fe-CSR (Fig. 1a).

The following describes a two-step preparation procedure for La-Fe-CSR (Fig. 1b). First, following the synthesis procedure described above, a suspension containing Fe-CSR was prepared. To the suspension, 50 mL of lanthanum nitrate solution (50 g/L) was added, and the pH (10.5) was adjusted using NaOH (1 mol/L). Then, the suspension was allowed to stabilize for an additional hour. Finally, La-Fe-CSR was obtained using the same collection method described earlier.

Characterization

A scanning electron microscope (SEM, SU8020, Hitachi High-Technologies Co, Japan) was used to analyze the surface morphology of the samples. Samples were analyzed for their elemental composition using an X-ray spectrometer (EDS, INCAENERGY350, UK). The relevant Brunauer-Emmet-Teller (BET) metrics of the samples were measured using a MicromeriticsASAP2460 system at 77 K. A vibrating sample magnetometer (VSM, MPMS-XL-7, Quantum Design, USA) was used to analyze the magnetic properties of the samples. The mineralogical composition of the samples was determined using X-ray diffraction (XRD, Bruker D8 ADVANCE, Germany). A zeta potential analyzer (Litesize DLS, Anton Paar, Austria) was employed to measure the surface charge of the samples. A Fourier Transform Infrared (FTIR) Spectroscopy (Nicolet 5700, USA) was used to analyze the chemical bonding of the samples. The binding energies of electrons in the samples were tested using X-ray photoelectron spectroscopy (XPS, Kratos AXIS Ultra, Kratos Analytical Ltd., Japan).

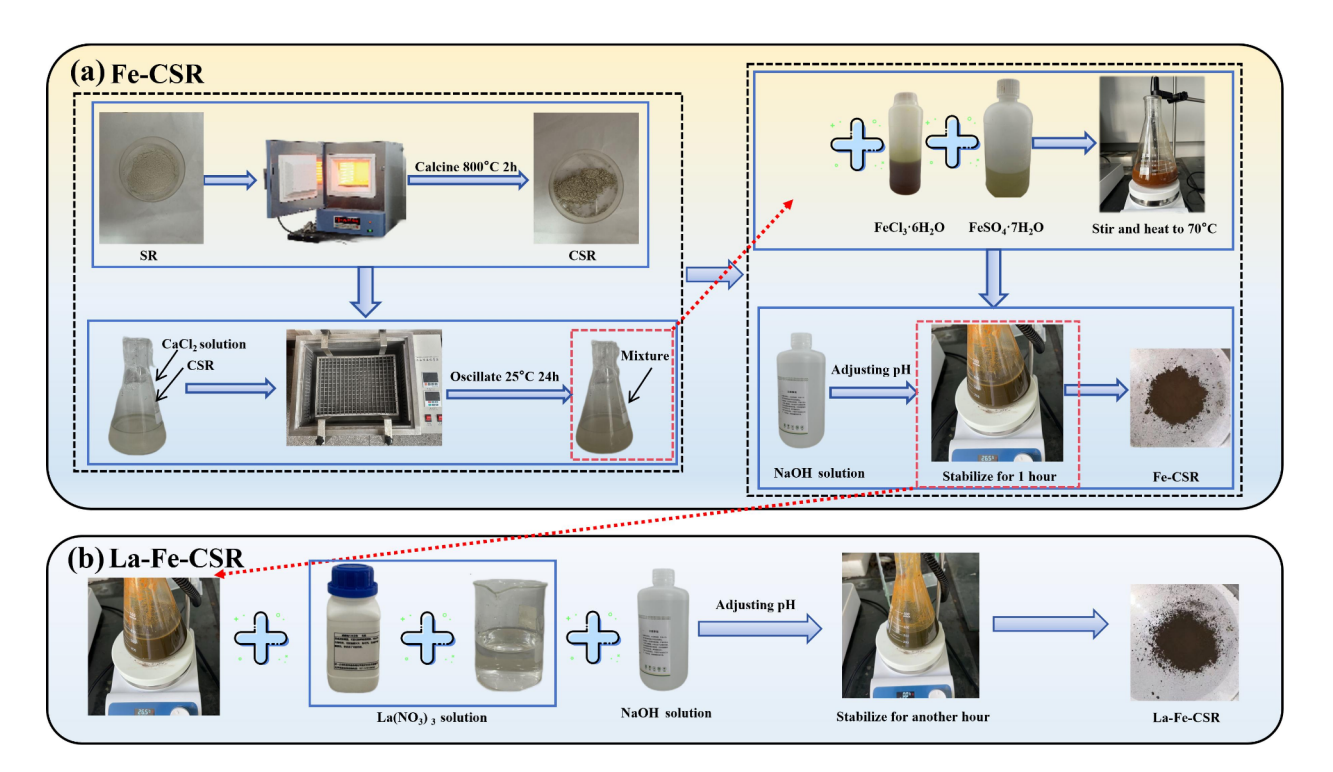


Fig. 1. Preparation flow chart. (a) Fe-CSR; (b) La-Fe-CSR.

Batch adsorption experiments

A specific amount of adsorbent (1 g/L) was added to a triangular flask containing 50 mL of phosphate solution. The pH was then adjusted using various concentrations of NaOH or HCl solutions (0.1–1 mol/L) and subsequently placed in a thermostatic shaker for 24 h (25 °C, 150 r/min). At the end of the reaction, the phosphate concentration was measured, and the phosphate uptake capacity (Q_p mg/g) and removal rate (R, %) were calculated using Eqs. (1–2). Each experiment was performed three times, and the error bars show±one standard deviation from the mean of these three trials.

$$Q_t = \left[\left(C_0 - C_t \right) / m \right] \times V \tag{1}$$

$$R = [(C_0 - C_t)/C_0] \times 100\%$$
(2)

Where C_0 (mg/L) and C_t (mg/L) represent the initial concentration and the concentration at time t (min), respectively, and m (g) and V (L) represent the adsorbent dosage and the solution volume, respectively.

The phosphate concentration in the solution was measured by adding adsorbent (1 g/L) to 50 mL of phosphate solution (20 mg/L), shaking for 24 h, and sampling at fixed intervals (0–1440 min). Experimental data were fitted using the pseudo-first (Eq. 3) and pseudo-second (Eq. 4) order kinetic model.

$$In\left(Q_e - Q_t\right) = InQ_e - k_1 t \tag{3}$$

$$t/Q_t = 1/k_2 Q_e + t/Q_e \tag{4}$$

where Q_e (mg/g) represents the adsorption capacity at equilibrium, k_1 (1/min) and k_2 (g/(mg min)) are the adsorption rate constants.

The adsorbent was added to phosphate solutions of varying concentrations (10–120 mg/L) to conduct adsorption isotherm experiments, with other conditions identical to those described previously. Langmuir (Eq. 5) and Freundlich (Eq. 6) models were utilized to analyze the experimental data.

$$Q_e = Q_m K_L C_e / (1 + K_L C_e) \tag{5}$$

$$Q_e = K_F C_e^{1/n} \tag{6}$$

where Q_m (mg/g) is the maximum capacity, C_e (mg/L) is the equilibrium concentration, and K_L , K_{F_0} and 1/n are constants.

The effect of initial pH (2.0–11.0) on phosphate adsorption (initial concentration of 60 mg/L) by the adsorbent was investigated. The selectivity of the adsorbent for phosphate (initial concentration of 50 mg/L) was investigated in the presence of coexisting ions $(SO_4^{\ 2^-},\ HCO_3^{\ -},\ Cl^-,\ NO_3^{\ -},\ Ca^{2^+},\ and\ Mg^{2^+})$ at different concentrations (50 mg/L and 100 mg/L).

The influence of temperature (288 K, 298 K, and 308 K) on the adsorbent's capacity was examined. The initial phosphate solution concentration was 50 mg/L. The equilibrium constant (K_D), Gibbs free energy (ΔG^0 , kJ/mol), enthalpy change (ΔH^0 , kJ/mol), and entropy change (ΔS^0 , J/(mol K)) were determined using Eqs. (7–9), T refers to the temperature in Kelvin (K), and R denotes the ideal gas constant (8.314 J/(mol K)).

$$K_D = \frac{Q_e}{C_e} \tag{7}$$

$$\Delta G^0 = -RTIn(K_D) \tag{8}$$

$$In\left(K_{D}\right) = -\frac{\Delta H^{0}}{RT} + \frac{\Delta S^{0}}{R} \tag{9}$$

Adsorbent continuous regeneration performance

To examine the continuous regeneration performance of the adsorbent, we performed five cycle experiments. 50 mg of La-Fe-CSR was added to 50 mL of a phosphate solution with a concentration of 50 mg/L and then reacted for 24 h. After each adsorption of phosphate, La-Fe-CSR was desorbed with NaOH (1 mol/L) solution²², then washed with deionized water, dried (105 °C), and ground for reuse in subsequent cycles.

Removal of phosphates from real domestic sewage

To evaluate the removal efficiency of adsorbents for real domestic sewage, domestic sewage collected from the dormitory building at Jiangsu Ocean University in Jiangsu Province was used as the test sample. 50 mg of La-Fe-CSR was added to 50 mL of domestic sewage and reacted for 24 h. Finally, the La-Fe-CSR in the domestic sewage was magnetically recovered, and the treated domestic sewage was analyzed for water quality.

Results and discussion Characterization of materials

The materials were characterized using SEM, EDS, BET, XRD, and VSM. Figure 2 presents the SEM and EDS images of SR, Fe-CSR, and La-Fe-CSR. As shown in Fig. 2a, a considerable number of lamellar crystals and relatively large pores could be observed on the SR surface. After modification, the surfaces of both Fe-CSR and La-Fe-CSR became very rough and possessed a large number of pores (Fig. 2b,c). We also found that both Fe-CSR and La-Fe-CSR surfaces were loaded with a large number of spherical particles, which were hypothesized to be related to the loading of Fe. Furthermore, compared with Fe-CSR, some short rods existed on the surface of La-Fe-CSR in addition to the spherical particles. It was hypothesized that the appearance of these short rods was related to the La modification²³.

The EDS scan of SR revealed that the main component of SR was CaCO₃ (Fig. 2d), which was consistent with the results of previous studies²⁴. Figure 2e confirmed the doping of Fe in Fe-CSR. Importantly, in La-Fe-CSR, both Fe and La were detected simultaneously (Fig. 2f), indicating that Fe and La oxides had been loaded onto the adsorbent, consistent with the SEM results. The total contents of La and Fe in La-Fe-CSR were 10.48% and 24.38%, respectively, which were lower than those reported in previous literature on La/Fe-based materials²⁰. Despite the low La content in La-Fe-CSR, the efficiency of La utilization can be improved. This is because the distribution of La tends to be more homogeneous in adsorbents with lower La content, enhancing the interaction with phosphate ions and leading to better phosphate uptake²⁵.

The pore structure of the adsorbent was further investigated. As shown in Fig. 3, the isotherms of both SR and La-Fe-CSR belong to the $\rm H_3$ -type hysteresis loop isotherm in the type IV isotherm, and the isotherms of adsorption and desorption of the two materials do not completely coincide with each other, suggesting that the two materials have a porous structure²⁶. This facilitates phosphate uptake as phosphate ions can be efficiently transported within the adsorbent. The pore size distribution, shown in the inset in Fig. 3, indicated that pore sizes of both SR and La-Fe-CSR were concentrated in the range of 2–75 nm, indicating a mainly mesoporous pore structure for both materials.

The results of BET calculations for SR, CSR, Fe-CSR, and La-Fe-CSR are provided in Table 1. Compared to SR $(34.04~\text{m}^2/\text{g})$, CSR $(42.35~\text{m}^2/\text{g})$ exhibited an increase of $8.31~\text{m}^2/\text{g}$ in specific surface area (SSA) after calcination, indicating that calcination improved the SSA of SR. The total pore volume increased slightly, but the average pore size decreased to $15.19~\text{m}^2/\text{g}$, which may result from the removal of surface-active substances or structural changes in SR during the calcination process. Compared to CSR, the SSA $(120.98~\text{m}^2/\text{g})$ of Fe-CSR further increased after Fe modification, suggesting that Fe can enhance the SSA of CSR. However, the average pore size of Fe-CSR increased to $16.04~\text{m}^2/\text{g}$, possibly due to the formation of new pore structures or expansion of existing pores during the Fe loading process. Notably, after La modification, the SSA of La-Fe-CSR reached $144.60~\text{m}^2/\text{g}$, suggesting that La modification significantly enhanced the SSA of Fe-CSR, thus providing more adsorption sites for phosphate adsorption. In addition, the total pore volume of La-Fe-CSR $(0.76~\text{cm}^2/\text{g})$ was significantly higher compared to SR $(0.15~\text{cm}^2/\text{g})$, attributed to the successful loading of Fe and La onto the surface of SR, followed by agglomeration²⁷.

Figure 4 shows the XRD and VSM images of SR, Fe-CSR, and La-Fe-CSR. As shown in Fig. 4a, the peaks at 23.1°, 29.4°, 36.0°, 39.4°, 43.2°, 47.4°, 48.5°, 57.5°, 60.4°, and 64.7° corresponded to CaCO $_3$, while peaks at 11.6°, 14.8°, 20.8°, and 56.6° were attributed to CaSO $_4$ (CaSO $_4$ ·0.5H $_2$ O and CaSO $_4$ ·2H $_2$ O)²⁸. These results indicated that SR primarily consisted of calcium-containing compounds, consistent with EDS analysis. Compared to SR, after Fe modification, prominent characteristic peaks appeared at 35.5°, 43.7°, 56.9° and 62.8°, which corresponded to the characteristic peaks of Fe $_3$ O $_4$, indicating that Fe was successfully loaded onto the surface of Fe-CSR and La-Fe-CSR. Remarkably, compared to Fe-CSR, distinct peaks were observed at 27.9° and 52.8°, consistent with

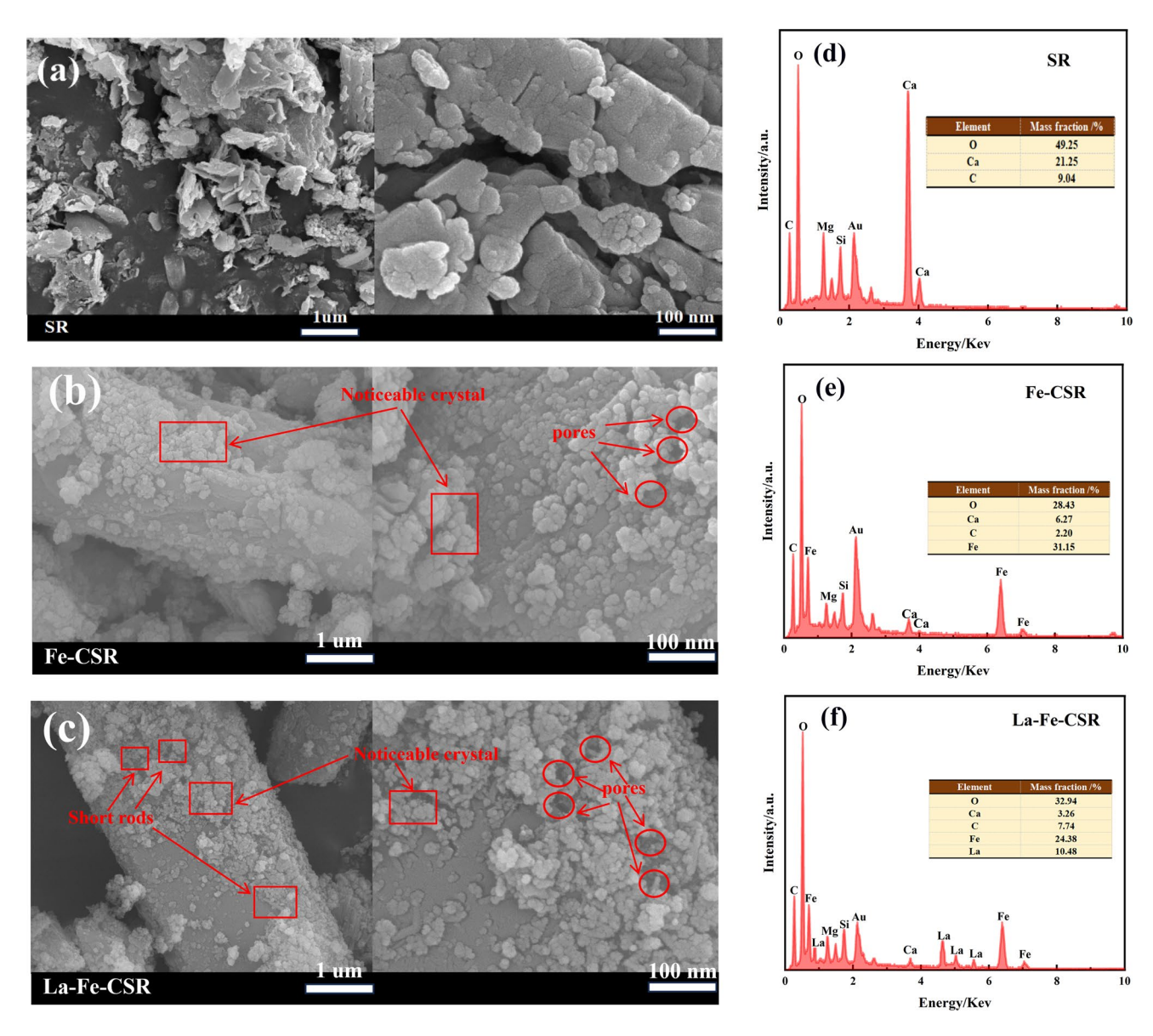


Fig. 2. SEM of SR (a), Fe-CSR (b), and La-Fe-CSR (c); EDS of SR (d), Fe-CSR (e), and La-Fe-CSR (f).

the characteristic peaks of La(OH)₃, suggesting that La on the surface of La-Fe-CSR existed in the form of La(OH)₃²⁹.

Magnetic field strength reflects the recyclability performance of magnetic adsorbents. The VSM test results of Fe-CSR and La-Fe-CSR are shown in Fig. 4b. The magnetic forces were 20.9 emµ/g for Fe-CSR and 17.2 emµ/g for La-Fe-CSR, respectively. Although the magnetic force of La-Fe-CSR exhibited some attenuation compared to Fe-CSR due to the loading of La, its magnetic property remained superior and could meet the criterion for the recycled magnetic force required for magnetic adsorbents. In the inset of Fig. 4b, it was evident that SR exhibited no response to magnetic force, while La-Fe-CSR could be effectively recycled from water using magnetism.

Effect of pH and coexisting ion

The effect of pH on the adsorption of phosphate by adsorbents is crucial as it directly affects the ionic form of phosphate and its chemical properties in aqueous solution. Figure 5a displays the morphology of phosphate ions at different pH levels. When the pH is below 2.15, the primary species in the solution is $\rm H_3PO_4$; between pH 2.15 and 7.20, it is predominantly $\rm H_2PO_4^{-}$; and from pH 7.20 to 12.33, it is mainly HPO $_4^{2-}$. Figure 5b illustrates the effect of pH on phosphate adsorption by La-Fe-CSR. Specifically, at a pH of 2, there was a weak electrostatic attraction between $\rm H_3PO_4$ and La-Fe-CSR, no ion exchange occurred, and the La loaded onto La-Fe-CSR was prone to leaching, resulting in poor adsorption efficiency³⁰. The adsorption of phosphate onto La-Fe-CSR increased significantly with increasing pH. This is because, within the pH range of 2–7, La on the surface of La-Fe-CSR undergoes a protonation reaction to form La-OH $_2^+$ (Eq. 10). At this point, due to the interaction between oxygen ions and anions, electrostatic attraction (Eq. 11) occurs between $\rm H_2PO_4^-$ and La-OH $_2^+$ in solution, thereby enhancing the adsorption of phosphate by La-Fe-CSR³¹. However, beyond pH 7, there was

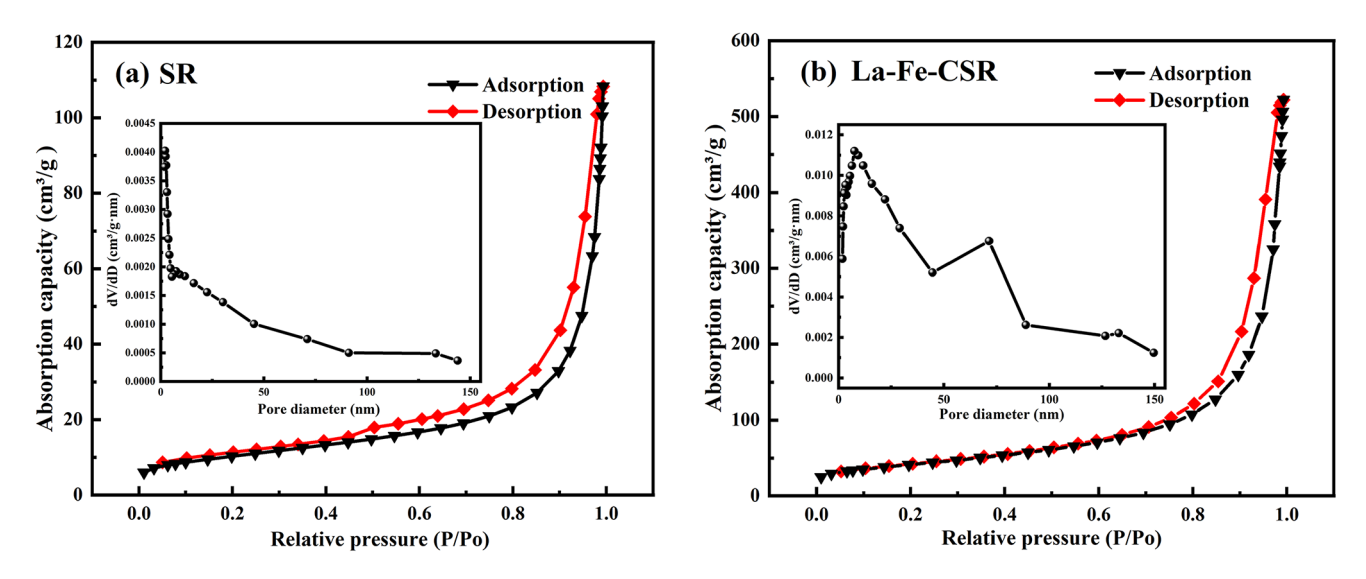


Fig. 3. Absorption and desorption isotherms for SR and La-Fe-CSR (inset shows pore size distribution curves).

Sample	BET surface area (m ² /g)	Total pore volume (cm ³ /g)	Average pore size (nm)	
SR	34.04	0.15	20.31	
CSR	42.35	0.20	15.19	
Fe-CSR	120.98	0.57	16.04	
La-Fe-CSR	144.60	0.76	21.04	

Table 1. The structural parameters of SR, CSR, Fe-CSR, and La-Fe-CSR.

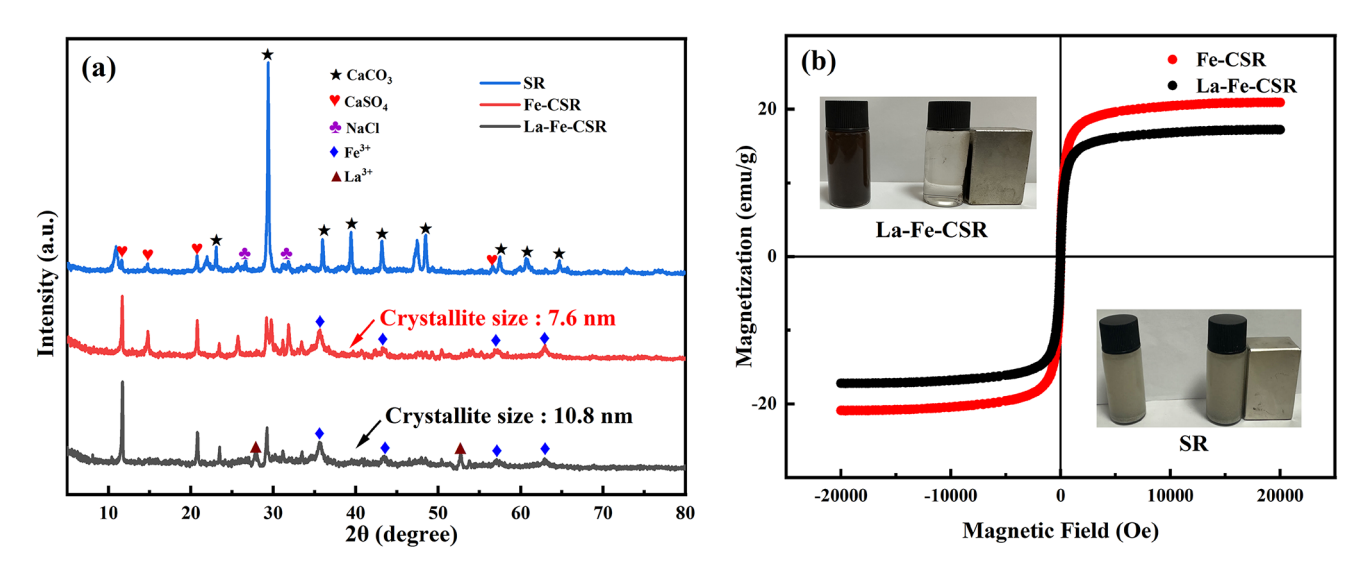


Fig. 4. (a) XRD of SR, Fe-CSR, and La-Fe-CSR; (b) VSM of Fe-SR and La-Fe-CSR (the inset displays the results of magnetic separation of SR and La-Fe-CSR under an applied magnetic field).

a gradual decline in phosphate adsorption, likely due to the low affinity of La for $\mathrm{HPO_4}^{2-}$ and the presence of numerous $\mathrm{OH^-}$ ions in solution, competing for adsorption sites with $\mathrm{HPO_4}^{2-}$. In addition, Fig. 5c shows the point of zero charge (PZC) of La-Fe-CSR is 6.25. This indicates that when the pH exceeds the PZC, the surface of La-Fe-CSR shifts from positive to negative³², generating an electrostatic repulsion effect. Consequently, the electrostatic attraction (Eq. 12) weakens, resulting in a decrease in adsorption capacity³³.

Furthermore, we observed an increase in solution pH after phosphate adsorption when the initial pH ranged from 2 to 9. This phenomenon may be attributed to the generation of OH⁻ when phosphate interacted with

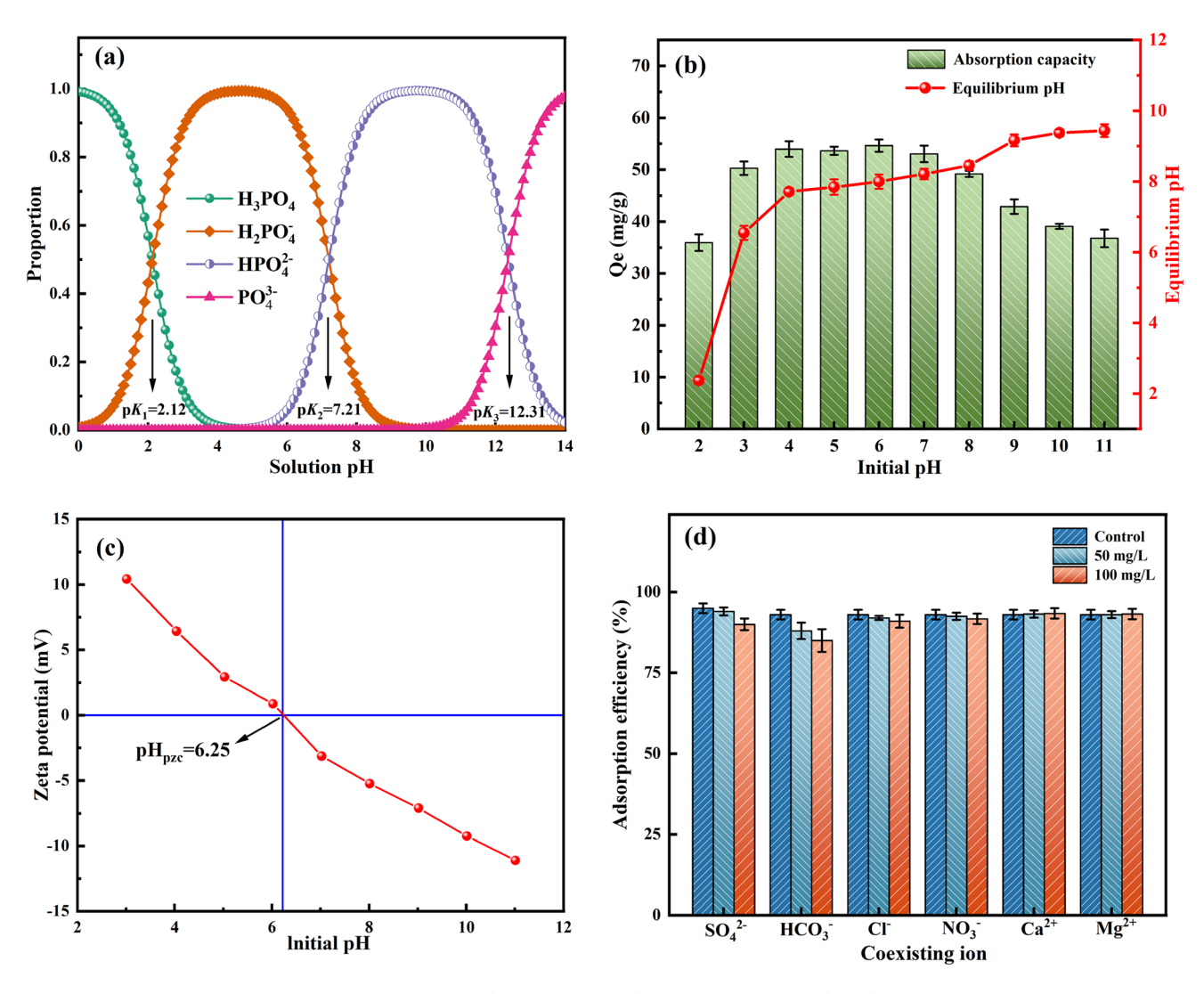


Fig. 5. Species distribution of phosphate at different pH levels (a), effect of pH (b), zeta potential analysis (c) and effect of coexisting ions on La-Fe-CSR (\mathbf{d}).

protonated lanthanum hydroxide via ligand exchange (Eqs. 13-14). Conversely, when the pH was greater than 9, the pH of the solution decreased instead after the adsorption of phosphate, which may have been due to the formation of LaO $^-$, the deprotonated form of La, which released H $^+$ ions (Eq. 15), thereby lowering the overall pH of the solution 23 . In summary, it was hypothesized that electrostatic interactions (non-specific) and ligand exchange (specific) were important mechanisms for phosphate removal by La-Fe-CSR. We will elaborate on the La-Fe-CSR adsorption mechanism in "Adsorption mechanisms" section.

$$La - OH + H^+ \leftrightarrow La - OH_2^+ \tag{10}$$

$$La - OH_2^+ + H_2PO_4^- \to (La - OH_2^+) + (H_2PO_4^-)$$
 (11)

$$La - OH_2^+ + HPO_4^{2-} \rightarrow (La - OH_2^+) + (HPO_4^{2-})$$
 (12)

$$La - OH + H_2PO_4^- \to La - H_2PO_4 + OH^-$$
 (13)

$$2La = OH + HPO_4^{2-} \rightarrow La_2 - HPO_4 + 2OH^-$$
 (14)

$$La - OH + H_2O \to LaO^- + H_3O^+$$
 (15)

$$Ca^{2+} + 2H_2PO_4^- + H_2O \to Ca(H_2PO_4)_2 \cdot H_2O$$
 (16)

$$Mg^{2+} + 2H_2PO_4^- \to Mg(H_2PO_4)_2$$
 (17)

High concentrations of competing ions may reduce adsorbent adsorption sites, thereby limiting phosphate removal efficiency. Therefore, it is crucial to consider these factors when designing and operating the adsorption

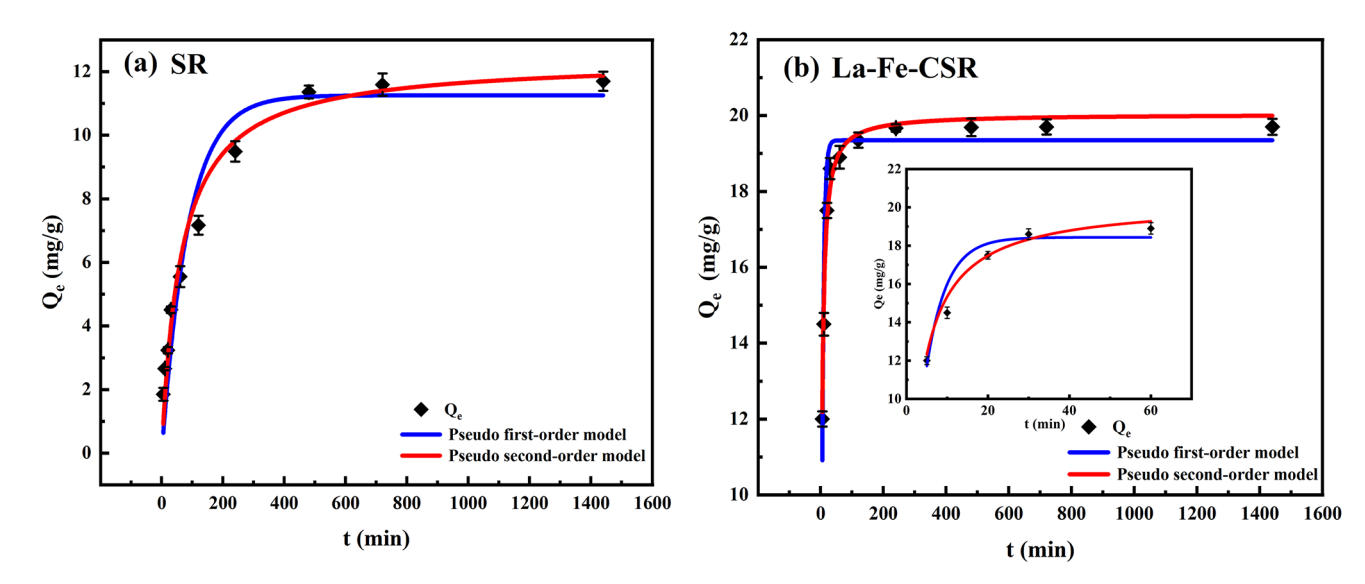


Fig. 6. Adsorption kinetic curves. (a) SR; (b) La-Fe-CSR (inset shows adsorption kinetic for the first 60 min).

		Pseudo-first-order kinetic			Pseudo-second-order kinetic			
Absorbents	T (°C)	k ₁ (1/min)	$q_e (\text{mg/g})$	R ²	$k_2 (g/(mg \cdot min))$	$q_e (\text{mg/g})$	R ²	
SR	25	0.0117	11.25	0.9240	0.0012	12.40	0.9707	
La-Fe-SR	25	0.1632	19.24	0.9231	0.0152	19.94	0.9864	

Table 2. Kinetic parameters of SR and La-Fe-CSR adsorption.

system to achieve the desired phosphate removal. Figure 5d illustrates the selectivity of La-Fe-CSR for varying concentrations of coexisting ions (SO_4^{2-} , HCO_3^{-} , Cl^{-} , NO_3^{-} , Ca^{2+} , and Mg^{2+}) during adsorption. NO_3^{-} and Cl^{-} ions exhibited minimal impact on phosphate removal by La-Fe-CSR. SO_4^{2-} reduced phosphate removal by approximately 4.1%, likely because SO_4^{2-} belongs to the multivalent anions, which are more readily adsorbed than monovalent anions³⁴. However, HCO_3^{-} significantly affected phosphate adsorption by La-Fe-CSR, reducing removal efficiency by about 8.3%, likely because the adsorbent has a stronger attraction to HCO_3^{-} than phosphate ions. Notably, Ca^{2+} and Mg^{2+} did not negatively affect phosphate adsorption by La-Fe-CSR but instead enhanced phosphate adsorption. This phenomenon may be attributed to the formation of a complex between phosphate in solution and the adsorption sites on the adsorbent through ligand exchange, which carries anions and can adsorb Ca^{2+} and Mg^{2+} . The adsorbed Ca^{2+} and Mg^{2+} also function as binding sites for phosphate ions (Eqs. 16 and 17). In general terms, La-Fe-CSR could resist most coexisting ions and exhibited high adsorption selectivity for phosphate, indicating that La-Fe-CSR holds promise for application in real sewage treatment. On this point, we will verify this in "Reusability of La-Fe-CSR" section.

Adsorption kinetics

The adsorption equilibrium time can significantly affect the performance, economy, and sustainability of the adsorption system, making it a crucial consideration in the design and optimization of the adsorption system. The adsorption kinetic fitting models for SR and La-Fe-CSR demonstrated distinct adsorption behaviors and efficiencies over time, as illustrated in Fig. 6. For SR, phosphate adsorption occurred primarily within the first 120 min, capturing 59.7% (6.98 mg/g) of the limit value. After this initial phase, the rate of adsorption slowed down, eventually reaching saturation around 480 min.

In contrast, La-Fe-CSR displayed a much more rapid adsorption process, with 73.2% (14.50 mg/g) of the adsorption limit value being achieved within the first 10 min. This indicated a significantly higher initial adsorption rate compared to SR. Following this swift uptake, the adsorption rate decreased, presumably due to the gradual filling of available adsorption sites on the La-Fe-CSR surface, with complete saturation reached approximately at 120 min. It was evident that the adsorption time for phosphate was greatly shortened after SR was modified. This could be attributed to the improvement of the electronic structure of La by Fe in La-Fe-CSR, thereby facilitating more efficient utilization of the active sites of La for rapid adsorption kinetics³⁵.

The parameters of the adsorption kinetic fitting models for SR and $\hat{L}a$ -Fe-CSR are shown in Table 2. The results indicated that the pseudo-second-order kinetic model effectively described the adsorption data of SR and La-Fe-CSR (R^2 =0.9707, R^2 =0.98864). Their theoretical adsorption limit values (12.40 mg/g, 20.03 mg/g) were close to the measured values (11.82 mg/g, 19.70 mg/g). This indicated that chemical adsorption was the primary process through which SR and La-Fe-CSR adsorb phosphate. In this process, the adsorbents and the adsorbate

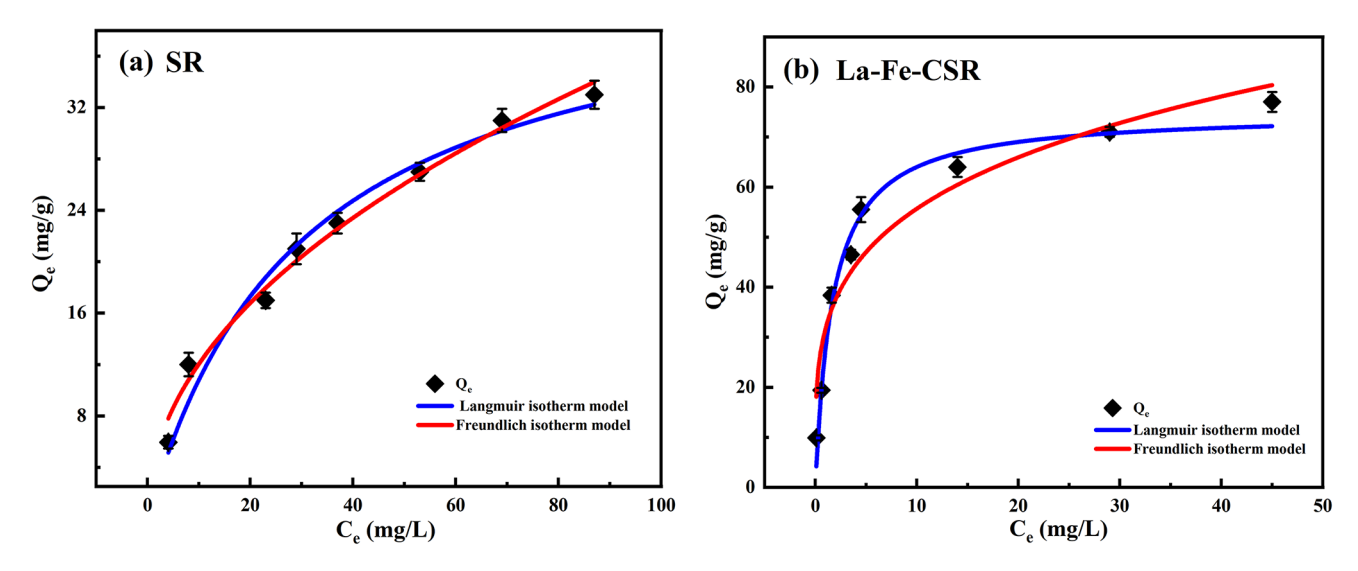


Fig. 7. Adsorption isotherms of SR (a) and La-Fe-CSR (b).

		Langmuir isotherm model			Freundlich isotherm model		
Absorbents	T (°C)	$q_m (\text{mg/g})$	K_L (L/mg)	R ²	K_F	1/n	R ²
SR	25	43.65	0.0331	0.9715	3.9844	0.4808	0.9843
La-Fe-CSR	25	74.87	0.5736	0.9793	31.5289	0.2442	0.9117

Table 3. Isotherm parameters of SR and La-Fe-CSR adsorption.

interact through electron sharing or exchange, typically involving phosphate replacing surface hydroxyl groups (–OH) and forming strong chemical bonds⁵.

Adsorption Isotherm

The adsorption isotherm is a crucial means for evaluating adsorbent performance and the adsorption behavior. An isotherm study was conducted to determine the adsorption properties of SR and La-Fe-CSR. Figure 7 shows the adsorption isotherm data for SR and La-Fe-CSR. The removal of phosphate by SR significantly decreased at high concentrations, with an adsorption capacity of only 32.27 mg/g. In contrast, the adsorption limit value of La-Fe-CSR was 75.12 mg/g, indicating that La/Fe incorporation effectively enhanced the adsorption capacity of SR³⁵.

The Langmuir and Freundlich models describe the adsorption behavior of the adsorbents, and the fitting results are shown in Table 3. The Langmuir model assumes that adsorption occurs on a homogeneous surface, with adsorption limited to a monolayer, whereas the Freundlich model assumes that the energy distribution of adsorption sites on the adsorbent surface is heterogeneous and that adsorption occurs in multiple layers. The R² value of the Freundlich model for SR (0.9843) was higher than that of the Langmuir model (0.9715), indicating that the Freundlich model better describes the removal of phosphate, with SR adsorbing phosphate through a multilayer adsorption mechanism. This result was consistent with previous studies on SR¹³. In contrast, the Langmuir model for La-Fe-CSR exhibited a higher R² (0.9793), suggesting that its phosphate adsorption follows a monolayer adsorption model, and the adsorption behavior was predominantly chemical rather than physical. This is common in La-based materials³⁶. Furthermore, based on the Langmuir model, the theoretical maximum adsorption capacity of La-Fe-CSR was 74.87 mg/g, which is significantly higher than the saturation adsorption capacities of many La-modified materials reported in previous studies (see Table 4). This indicates that La-Fe-CSR demonstrates superior performance in phosphate adsorption. In addition, we evaluated the preparation cost of La-Fe-CSR. Based on market prices, the cost of the primary raw material for synthesizing La-Fe-CSR is approximately 60.69 USD/kg. This cost is relatively moderate compared to most La-based materials but still higher than that of La/Fe oxide composites and SAILa@AB, which cost 23.85 USD/kg and 37.98 USD/kg, respectively. Such a cost may limit the commercialization potential of La-Fe-CSR. Therefore, optimizing the synthesis process of La-Fe-CSR to reduce costs will be a key focus of our future research.

Adsorption thermodynamics

The effect of temperature on the adsorption capacities of SR and La-Fe-CSR is presented in Fig. 8. The results demonstrated that the adsorption capacities of SR and La-Fe-CSR increased as the temperature rose from 288 K to 308 K. This suggested that higher temperatures enhance the adsorption capacity of the adsorbent. SR exhibited a greater temperature dependence, particularly at 288 K, where the adsorption capacity was only

Materials	Adsorption capacity (mg/g)	Initial concentration (mg/L)	Temperature (°C)	Dosage (g/L)	Cost USD/kg	References
La-Fe-CSR	74.87	10-120	25	1	60.69	This work
La/Fe oxide composites	77.19	10-200	25	0.4	23.85	47
Fe ₃ O ₄ /La(OH) ₃	53.85	0.5-250	25	0.1	124	48
La ₂ O ₂ CO ₃ /γ-Fe ₂ O ₃	134.82	5–100	25	0.2	99.29	49
LC-MC	34.20	10-200	25	1.5	79.96	50
SAILa@AB	21.30	10-1000	25	10	37.98	51

Table 4. Comparison of La-based absorbents for phosphorus removal capacity.

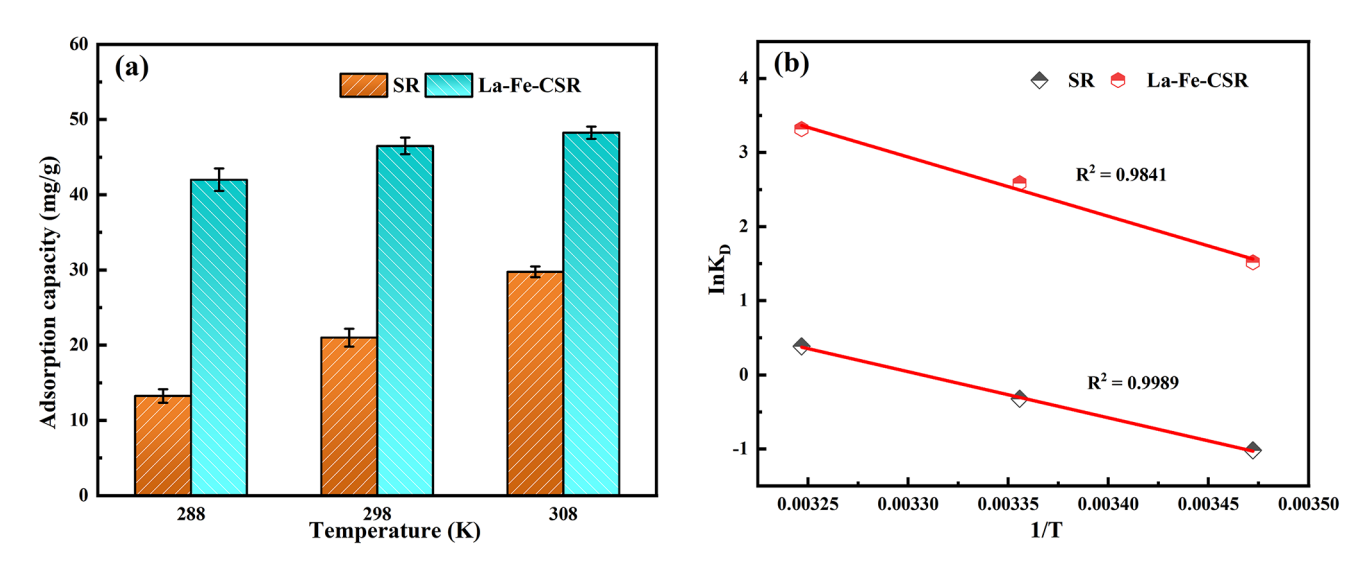


Fig. 8. Temperature influence on adsorption (a) and thermodynamic constants graph (b).

	ΔG ⁰ (kJ/mol)				
Absorbents	288 K	298 K	308 K	ΔH ⁰ (kJ/mol)	ΔS ⁰ (J/(mol K))
SR	2.44	0.79	-0.99	51.78	171.23
La-Fe-CSR	-3.63	-6.41	-8.49	66.50	243.90

Table 5. Isotherm parameters of SR and La-Fe-CSR adsorption.

13.25 mg/g. In contrast, the adsorption capacity of La-Fe-CSR slightly decreased to 41.02 mg/g at 288 K. The adsorption thermodynamic data presented in Fig. 8b were further analyzed to derive the thermodynamic parameters. From Table 5, it can be observed that the ΔG^0 values for SR were positive at 288 K and 298 K, indicating a non-spontaneous adsorption process. However, at 308 K, the ΔG^0 value became negative, indicating a spontaneous adsorption process for SR at higher temperatures. The ΔG^0 values of La-Fe-CSR were negative at different temperatures, indicating that the phosphate adsorption process of La-Fe-CSR had a good spontaneous response, which is a common behavior in La-based materials³⁷. The positive ΔH^0 values of SR (51.78 kJ/mol) and La-Fe-CSR (66.50 kJ/mol) further indicated that the phosphate adsorption process of both materials was a thermoabsorptive reaction, and the high temperatures helped the phosphate removal. In addition, the positive values of ΔS^0 for SR (171.23 J/(mol K)) and La-Fe-CSR (243.90 J/(mol K)) indicate that the adsorption of phosphate by these two materials is in the direction of entropy increase, i.e., the interfacial randomness between the solids and the solution increases in the reaction process³⁸.

Adsorption mechanisms

FTIR analysis

Figure 9 displays the FTIR spectra of the adsorbent. As shown in Fig. 9a, the peaks at 3410 cm⁻¹ and 1620 cm⁻¹ correspond to the characteristic –OH stretching vibrational peaks²². The O–C–O stretching vibrational bands of SR at 1460 cm⁻¹ and 874 cm⁻¹ correspond to the presence of the CaCO₃ phase, and an O–S–O asymmetric stretching band can be clearly observed at 1149 cm⁻¹, indicating the presence of the CaSO₄ phase in SR. Compared with SR, the characteristic peaks of La-Fe-CSR at 3410 cm⁻¹ and 1620 cm⁻¹ were significantly enhanced, indicating that the number of –OH groups coordinated to La and Fe in the interlayer of SR increased after the loading of La and Fe, providing more adsorption sites for La-Fe-CSR. Characteristic peaks of Fe(OH)₃

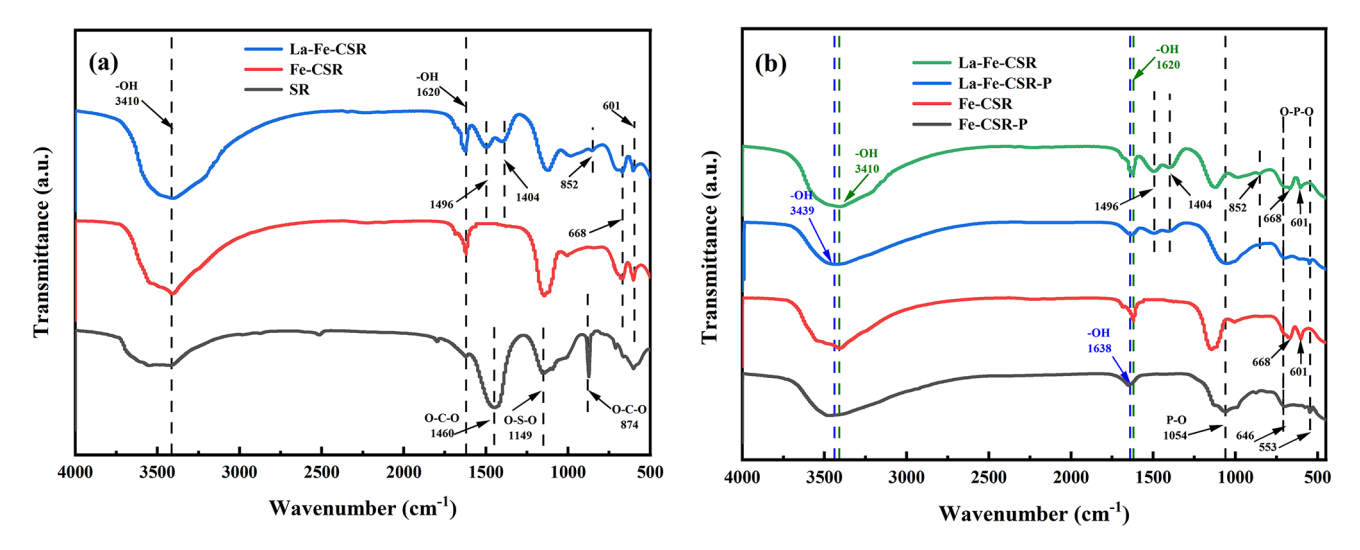


Fig. 9. FTIR spectra of SR, Fe-CSR, and La-Fe-CSR.

and Fe–O bonds were observed near 668 cm $^{-1}$ and 601 cm $^{-1}$, indicating that Fe was effectively loaded onto Fe-CSR and La-Fe-CSR. In addition, compared to Fe-CSR, the peaks at 1496 cm $^{-1}$ and 1404 cm $^{-1}$ correspond to La(OH) $_3$ ³⁹, suggesting that La is loaded as La(OH) $_3$ on the surface of La-Fe-CSR, consistent with the XRD analysis. The small peak observed near 852 cm $^{-1}$ may have been attributed to La-O.

As shown in Fig. 9b, after phosphate adsorption, the peaks of Fe-CSR and La-Fe-CSR at 3410 cm⁻¹ and 1620 cm⁻¹ not only shifted to higher wavebands (3439 cm⁻¹ and 1638 cm⁻¹) but also weakened, suggesting –OH involvement in phosphate adsorption. The appearance of new asymmetric vibrational peaks near 1054 cm⁻¹ corresponded to P–O bonding (HPO $_4$ ²⁻ or H $_2$ PO $_4$ ⁻). This observation was consistent with previous results⁴⁰, confirming that both adsorbents successfully adsorbed phosphate. The peaks at 646 cm⁻¹ and 553 cm⁻¹ for La-Fe-CSR corresponded to the O–P–O bending vibration. In addition, the iron hydroxide and Fe–O peaks of Fe-CSR and La-Fe-CSR disappeared at the end of the adsorption process, likely due to the involvement of Fe in phosphate adsorption⁴¹.

XPS analysis

To better understand the adsorbent-phosphate interactions, the adsorbent was analyzed by XPS (Fig. 10). Full-size images of P, La, Fe, O, and C are provided in Fig. 10a. Before the adsorption of O, Fe, C, and La were present in the XPS image of La-Fe-CSR, indicating that La and Fe were effectively synthesized on the surface of La-Fe-CSR. After adsorption, P signals were found in the full-size images, confirming the effective adsorption of phosphate by La-Fe-CSR. The P 2p peak spectra of La-Fe-CSR are shown in Fig. 10b. There is a distinct peak at 133.48 eV, referenced to the P 2p peak in KH₂PO₄ (134 eV)⁴², which is shifted toward the low-energy region. This shift is attributed to the ligand exchange between the adsorbent and phosphate (Eqs. 14–15). Additionally, with reference to the peaks of LaPO₄·xH₂O (132.88 eV) and FePO₄·2H₂O (133.60 eV), the P 2p peak (133.48 eV) of La-Fe-CSR was very close to them. This confirmed the formation of Fe-P complexes or La-P complexes. Some H₃PO₄ analogs had been identified, which had been produced through the reaction of LaPO₄ via the absorption of phosphate through –OH bonds (Eq. 18). Therefore, it was inferred that precipitation was one of the pathways for phosphate removal by La-Fe-CSR⁴³.

$$La^{3+} + PO_4^{3-} \rightarrow LaPO_4 \tag{18}$$

$$Fe - OH + H_2PO_4^- \to Fe - H_2PO_4^- + OH^-$$
 (19)

$$2Fe = OH + HPO_4^{2-} \to Fe_2 - HPO_4 + 2OH^-$$
 (20)

Shifting towards the high-energy region, La 3d_{3/2} and La 3d_{5/2} of La-Fe-CSR in Fig. 10c moved from 851.98 eV and 835.18 eV to 852.36 eV and 835.52 eV after phosphate loading. This shift, frequently observed in La-based materials, may be attributed to electron transfer within the La valence band⁴⁴. The Fe 2p_{3/2} (724.98 eV) and Fe 2p_{5/2} (711.38 eV) peaks of La-Fe-CSR shifted towards lower energies to 724.82 eV and 711.22 eV, respectively, after phosphate adsorption, with a shift of only 0.16 eV. This further suggests that Fe also served as a site for phosphate adsorption (Eqs. 19–20). The O 1s photoelectron spectroscopy data of La-Fe-CSR were deconvoluted based on oxygen binding energies to identify M–O, M–OH, and H₂O peaks. The valence band area of the M–O peak of La-Fe-CSR rose from 17.89 to 24.14% after phosphate loading, indicating that phosphate was adsorbed and existed on the surface of the adsorbent in the form of M–O–P⁴⁵. The valence band area of the M–OH peak declined from 61.11 to 43.32%, demonstrating that La-Fe-CSR binds phosphate by displacing –OH groups through ligand exchange. The ratio of the area of the M–OH valence band before and after the adsorption of La-Fe-CSR was approximately 1.41, falling within the range of 0.5 to 2.0⁴⁶ We hypothesized that La-Fe-CSR may form mononuclear monodentate and binuclear bidentate complexes in the course of phosphate sequestration.

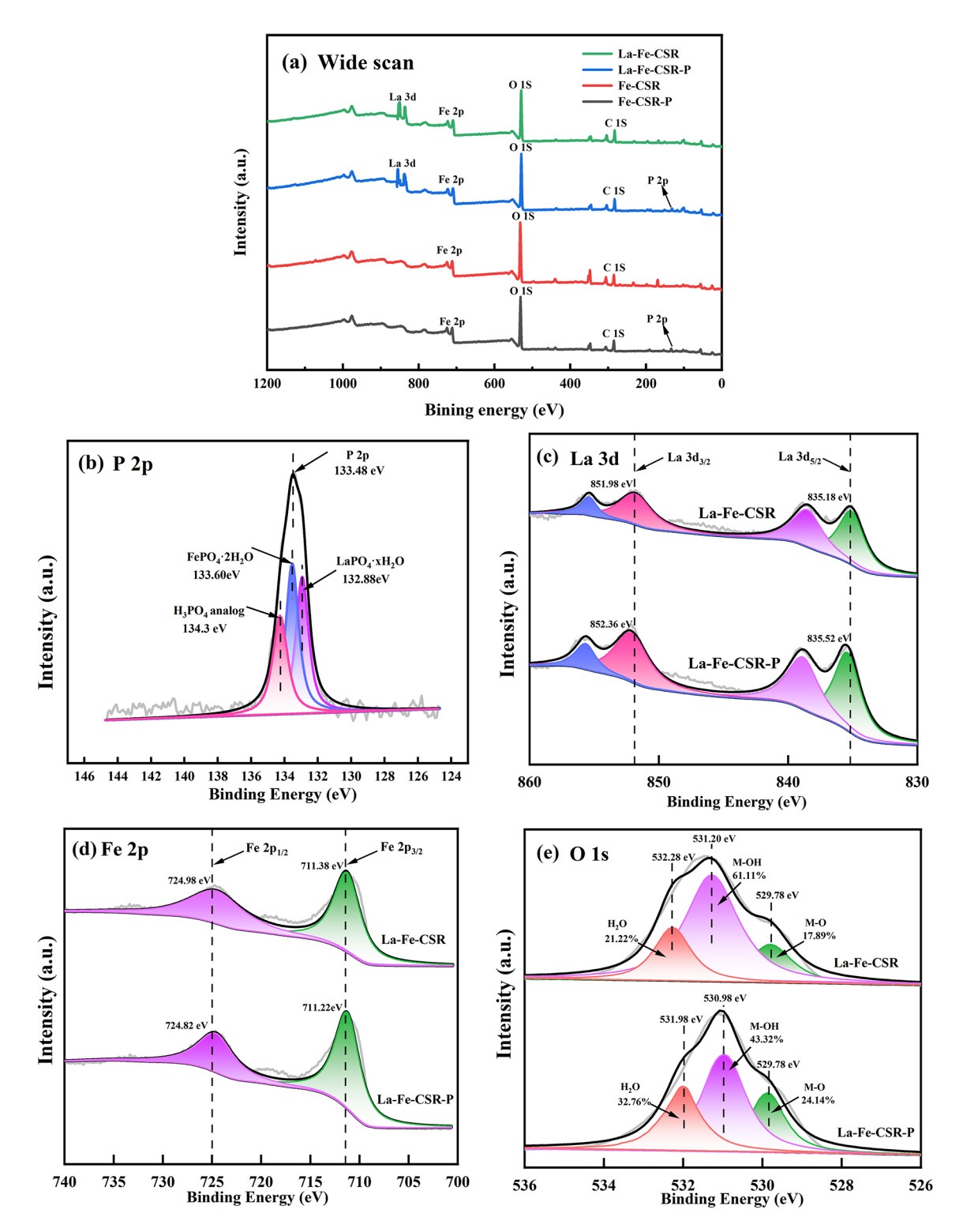


Fig. 10. XPS spectra of Fe-CSR and La-Fe-CSR before and after adsorption.

Combining all the obtained results, multiple adsorption mechanisms were involved in the phosphate uptake of La-Fe-CSR. La-Fe-CSR relies primarily on La to adsorb phosphate, while Fe may react with a small amount of phosphate to form complexes. Figure 11 illustrates the potential removal mechanisms involved in the phosphate removal process of La-Fe-CSR.

Reusability of La-Fe-CSR

Evaluating the utility and cost-efficiency of adsorbents depends largely on their cyclic regeneration performance, which was one of the focuses of La-Fe-CSR in this study. Figure 12a illustrates that La-Fe-CSR maintained

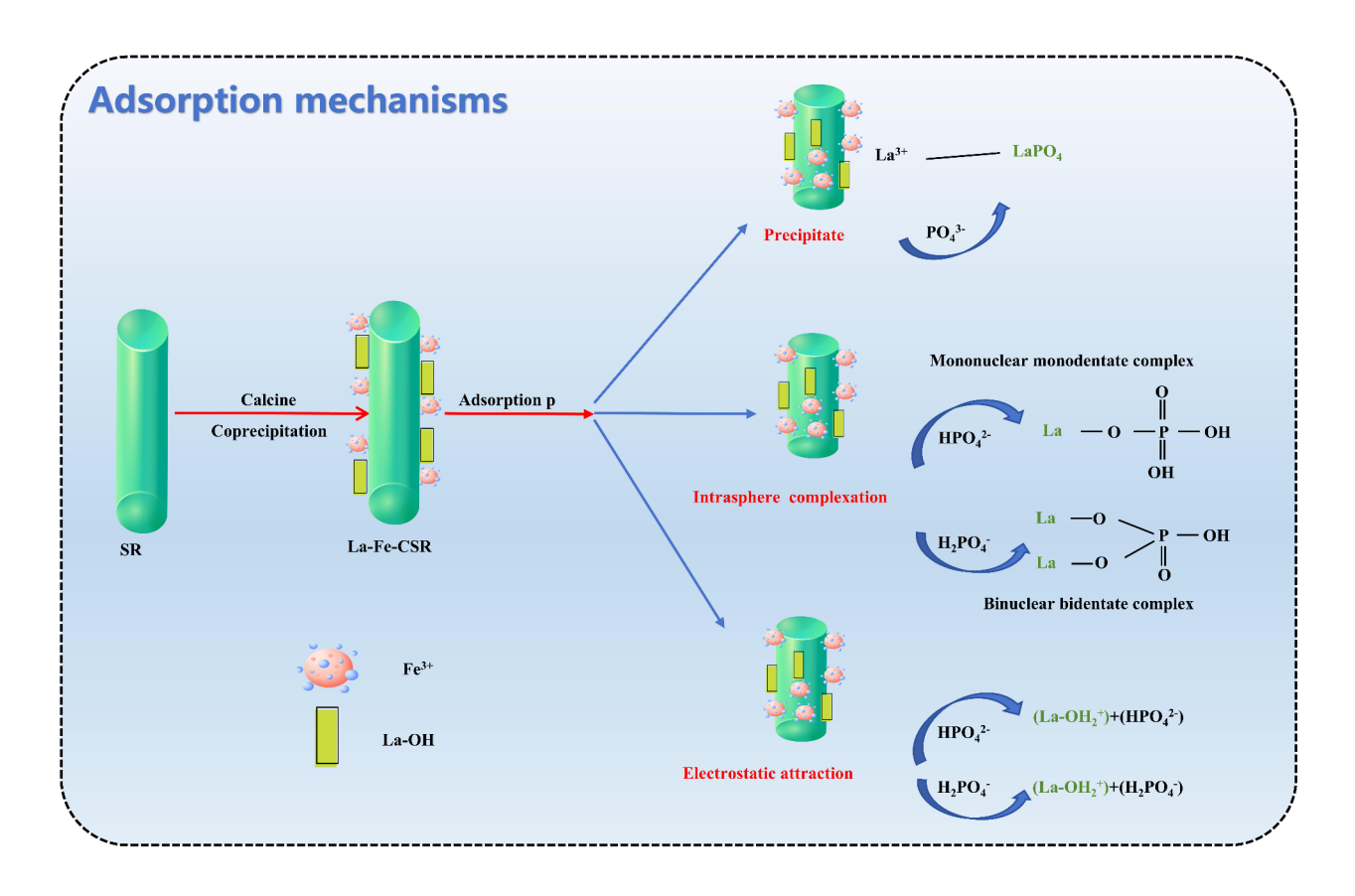


Fig. 11. The mechanism chart of phosphate adsorption by La-Fe-CSR.

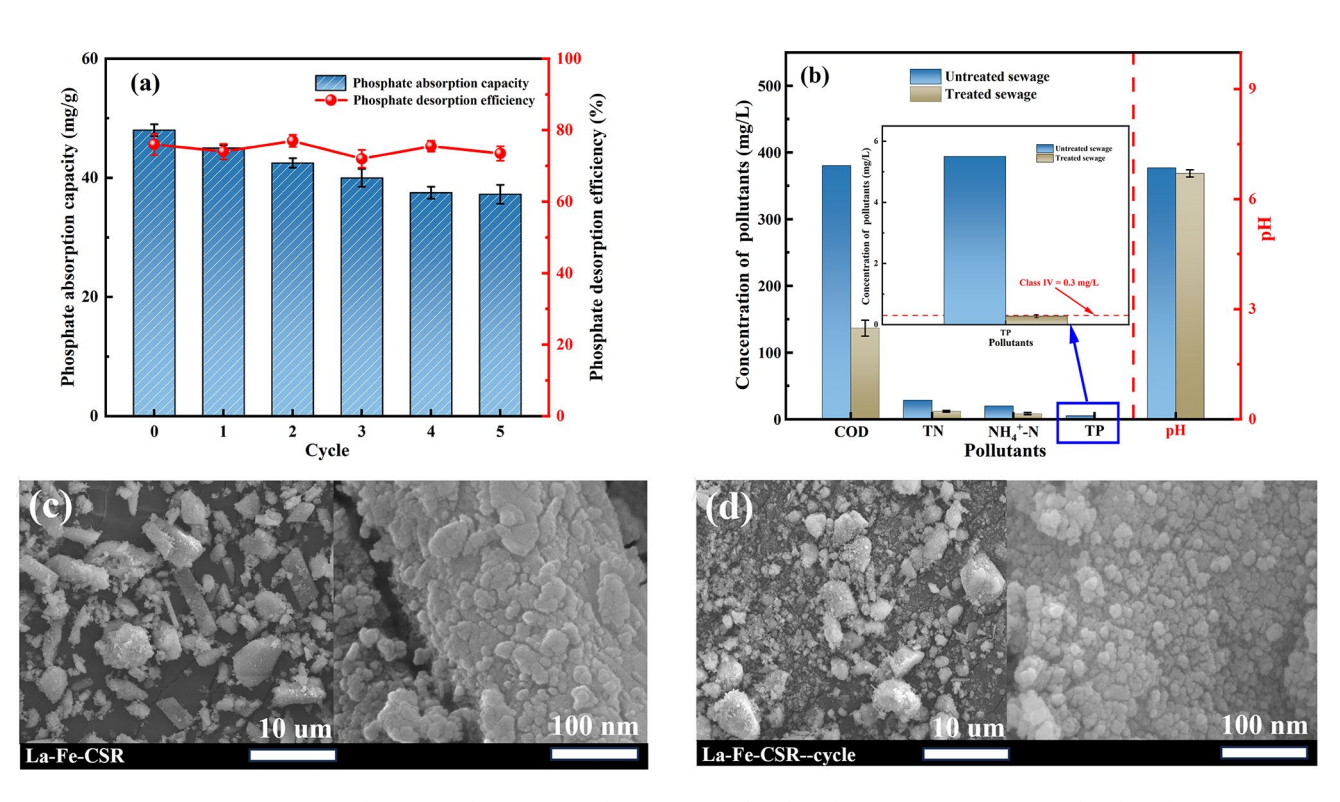


Fig. 12. Adsorption—desorption cycle experiment for phosphate (a); Concentration of each pollutant in sewage after La-Fe-CSR treatment (b); SEM images of La-Fe-CSR before and after cycling (**c**,**d**).

a robust adsorption rate of 89.2% for phosphate after the initial cycling test. Even after 5 cycles, La-Fe-CSR maintained an adsorption rate exceeding 74.5%. The decline in the phosphate adsorption capacity of La-Fe-CSR may be attributed to the permanent occupancy of active sites during subsequent cycles⁵¹. Figure 12(c-d) presents SEM images of La-Fe-CSR before and after cycling. As shown in Fig. 12c, compared to the SEM image taken before cycling, the La-Fe-CSR surface exhibited an increase in crystal formation after several cycles (Fig. 12d). Additionally, the pore structure appeared to become tighter. Based on these observations, we hypothesized that the increased crystallization and pore closure resulted from the formation of stronger chemical bonds between the phosphate and the lanthanide-based adsorbent. This process likely filled the pores and led to the permanent loss of some of the adsorbent's active sites. Furthermore, phosphate desorption efficiency consistently exceeded 70% across all five cycles. This indicated that La-Fe-CSR possessed the capability to recover phosphate despite repeated usage.

Real domestic sewage adsorption experiments

To address river eutrophication, sewage facilities are mandated to meet stringent phosphate limits, such as the environmental quality standard for surface water (Class IV = 0.30 mg/L). We evaluated the ability of La-Fe-CSR to treat domestic sewage. The parameters of the fresh domestic sewage were as follows: pH = 6.85, COD = 380.16 mg/L, TN = 28.52 mg/L, NH $_4$ +-N = 19.85 mg/L, and TP = 5.50 mg/L. Figure 12b illustrates the concentrations of each pollutant in the sewage following treatment with La-Fe-CSR. The concentration of TP in the actual sewage dropped from 5.50 mg/L to 0.28 mg/L, which falls below the Class IV environmental standard (0.30 mg/L). La-Fe-CSR also had a certain purification effect on COD, TN, and NH $_4$ +-N in domestic sewage, reducing their concentrations to 136.50 mg/L, 11.97 mg/L, and 8.52 mg/L, respectively. Although its performance in treating actual sewage was marginally less effective compared to lab-prepared phosphate solutions, likely due to the complexity of the sewage composition, the removal efficiency still reached 94.9%. These experimental results demonstrated the substantial potential of La-Fe-CSR as a highly efficient and rapid phosphate adsorbent.

Conclusions

La-Fe-CSR materials were synthesized and applied for the adsorption and recovery of phosphate from water. La-Fe-CSR exhibited superior phosphate removal within the pH range of 4–7. La-Fe-CSR had better resistance to coexisting ions. The adsorption kinetics and isotherms indicated that the adsorption process of La-Fe-CSR involved monolayer adsorption and chemisorption, respectively. The adsorption mechanisms of La-Fe-CSR for phosphate removal involved precipitation, electrostatic attraction, ligand exchange and complexation interactions. Moreover, La-Fe-CSR maintained over 74.5% adsorption efficiency and 70.0% desorption efficiency after five cycles of phosphate adsorption-desorption. Following treatment with La-Fe-CSR, the TP concentration in the domestic sewage was 0.28 mg/L, below the environmental quality standard for Class IV surface water (0.30 mg/L). In conclusion, our results not only promote the use of La-based adsorbents but also provide new ideas for the rational utilization of SR.

Limitations of the study

Although the La-Fe-CSR synthesized in this study demonstrates strong potential for phosphorus removal from domestic sewage, there are several limitations. These include: (1) the focus of this study was solely on phosphorus removal in domestic sewage, without examining its performance in more complex water bodies, such as industrial wastewater; (2) the study only investigated the removal of phosphorus as a single pollutant; and (3) the experimental conditions were confined to laboratory settings. As a next step, future research will aim to optimize the preparation process of La-Fe-CSR, explore its ability to synergistically remove other pollutants, and assess its long-term stability in various water bodies through pilot-scale experiments.

Data availability

The datasets used and/or analyzed during the current study are available from the corresponding author upon reasonable request.

Received: 11 August 2024; Accepted: 21 January 2025

Published online: 24 January 2025

References

- 1. d'Haese, P. C. et al. Human health risk associated with the management of phosphorus in freshwaters using lanthanum and aluminium. *Chemosphere* 220, 286–299. https://doi.org/10.1016/j.chemosphere.2018.12.093 (2019).
- Xu, R., Zhang, M., Mortimer, R. J. & Pan, G. Enhanced phosphorus locking by novel lanthanum/aluminum-hydroxide composite: Implications for eutrophication control. *Environ. Sci. Technol.* 51, 3418–3425. https://doi.org/10.1021/acs.est.6b05623 (2017).
- 3. Wang, Z., Shen, D., Shen, F. & Li, T. Phosphate adsorption on lanthanum loaded biochar. *Chemosphere* 150, 1–7. https://doi.org/10.1016/j.chemosphere.2016.02.004 (2016).
- 4. Xu, H. et al. Contributions of external nutrient loading and internal cycling to cyanobacterial bloom dynamics in Lake Taihu, China: Implications for nutrient management. *Limnol. Oceanogr.* 66, 1492–1509. https://doi.org/10.1002/lno.11700 (2021).
- 5. Mueller, D. K. & Helsel, D. R. Nutrients in the Nation's Waters: Too Much of a Good Thing? Vol. 1136 (US Government Printing Office, 1996).
- 6. Wu, D., Zhan, Y., Lin, J., Zhang, Z. & Xie, B. Contrasting effect of lanthanum hydroxide and lanthanum carbonate treatments on phosphorus mobilization in sediment. *Chem. Eng. J.* 427, 132021. https://doi.org/10.1016/j.cej.2021.132021 (2022).
- 7. Jiang, W. et al. Reuse of phosphogypsum and phosphorus ore flotation tailings as adsorbent: The adsorption performance and mechanism of phosphate. *J. Phys. Chem. Solids* 178, 111313. https://doi.org/10.1016/j.jpcs.2023.111313 (2023).
- Liu, L. & Zhang, M. Soda residue as a novel modifier for straw biochar enhanced recovery of phosphate and ammonium from water. Int. J. Environ. Sci. Technol. 20, 13783–13798. https://doi.org/10.1007/s13762-023-04935-4 (2023).

- 9. Dithmer, L., Nielsen, U. G., Lundberg, D. & Reitzel, K. Influence of dissolved organic carbon on the efficiency of P sequestration by a lanthanum modified clay. *Water Res.* **97**, 39–46. https://doi.org/10.1016/j.watres.2015.07.003 (2016).
- Li, X. et al. A novel red mud adsorbent for phosphorus and diclofenac removal from wastewater. J. Mol. Liq. 303, 112286. https://doi.org/10.1016/j.molliq.2019.112286 (2020).
- 11. Guo, W. et al. Mechanical properties and compressive constitutive relation of solid waste-based concrete activated by soda residue-carbide slag. Constr. Build. Mater. 333, 127352. https://doi.org/10.1016/j.conbuildmat.2022.127352 (2022).
- 12. Zong, Y. et al. Research status of soda residue in the field of environmental pollution control. RSC Adv. 13, 28975–28983. https://doi.org/10.1039/D3RA04863B (2023).
- 13. Yan, Y. et al. Removal of phosphate from wastewater using alkaline residue. *J. Environ. Sci.* 26, 970–980. https://doi.org/10.1016/S 1001-0742(13)60537-9 (2014).
- Wang, Q. et al. Preparation of soda residue-based geopolymer and phosphorus removal performance. Non-Met. Mines. 45, 76–81. https://doi.org/10.3969/j.issn.1000-8098.2022.03.020 (2022).
- 15. Yan, Y. et al. Removal of phosphate from etching wastewater by calcined alkaline residue: Batch and column studies. *J. Taiwan Inst. Chem. Eng.* 45, 1709–1716. https://doi.org/10.1016/j.jtice.2013.12.023 (2014).
- Wang, Y. et al. Effect of magnetic zirconium/iron-modified bentonite addition on phosphorus mobilization and species transformation in river sediments. Environ. Sci. 40, 649–657. https://doi.org/10.13227/j.hjkx.201806220 (2019).
- 17. Qu, Y. et al. Study on the management efficiency of lanthanum/iron co-modified attapulgite on sediment phosphorus load. *Chemosphere* 313, 137315. https://doi.org/10.1016/j.chemosphere.2022.137315 (2023).
- 18. Lu, C. et al. High affinity lanthanum doped iron oxide nanosheets for phosphate removal. Chem. Eng. J. 422, 130009. https://doi.org/10.1016/j.cej.2021.130009 (2021).
- 19. Xie, J. et al. Removal and recovery of phosphate from water by lanthanum hydroxide materials. Chem. Eng. J. 254, 163–170. https://doi.org/10.1016/j.cej.2014.05.113 (2014).
- Lin, J., Zhao, Y., Zhan, Y. & Wang, Y. Control of internal phosphorus release from sediments using magnetic lanthanum/iron-modified bentonite as active capping material. Environ. Pollut. 264, 114809. https://doi.org/10.1016/j.envpol.2020.114809 (2020).
- Wang, H. et al. Operational effect of green roof systems with a modified substrate adding soda residue soil. Water Supply 24, 1243–1253. https://doi.org/10.2166/ws.2024.070 (2024).
- 22. Luo, Q., Wei, J., Guo, Z. & Song, Y. Adsorption and immobilization of phosphorus from water and sediments using a lanthanum-modified natural zeolite: Performance, mechanism and effect. Sep. Purif. Technol. 329, 125187. https://doi.org/10.1016/j.seppur.20 23.125187 (2024).
- 23. Liu, Y., Huang, L., Le, X. & Huang, R. Performance and mechanism on the phosphorus adsorption by magnetic lanthanum-loaded acidified vermiculite. *J. Civ. Environ. Eng.* 46, 197–205. https://doi.org/10.11835/j.issn.2096-6717.2021.247 (2024).
- Wang, Q. et al. Characterization of the mechanical properties and microcosmic mechanism of Portland cement prepared with soda residue. Constr. Build. Mater. 241, 117994. https://doi.org/10.1016/j.conbuildmat.2019.117994 (2020).
- 25. Lan, Z., Lin, Y. & Yang, C. Lanthanum-iron incorporated chitosan beads for adsorption of phosphate and cadmium from aqueous solutions. Chem. Eng. J. 448, 137519. https://doi.org/10.1016/j.cej.2022.137519 (2022).
- Cui, R., Ma, J., Jiao, G. & Sun, R. Efficient removal of phosphate from aqueous media using magnetic bimetallic lanthanum-iron-modified sulfonylmethylated lignin biochar. *Int. J. Biol. Macromol.* 247, 125809. https://doi.org/10.1016/j.ijbiomac.2023.125809 (2023).
- 27. Shi, W. et al. Enhanced phosphate removal by zeolite loaded with Mg-Al-La ternary (hydr) oxides from aqueous solutions: Performance and mechanism. Chem. Eng. J. 357, 33-44. https://doi.org/10.1016/j.cej.2018.08.003 (2019).
- 28. An, Q., Pan, H., Zhao, Q., Du, S. & Wang, D. Strength development and microstructure of recycled gypsum-soda residue-GGBS based geopolymer. *Constr. Build. Mater.* 331, 127312. https://doi.org/10.1016/j.conbuildmat.2022.127312 (2022).
- Yuan, L. et al. Development of lanthanum hydroxide loaded on molecular sieve adsorbent and mechanistic study for phosphate removal. J. Alloys Compd. 768, 953–961. https://doi.org/10.1016/j.jallcom.2018.07.230 (2018).
- 30. He, Y., Lin, H., Dong, Y., Liu, Q. & Wang, L. Simultaneous removal of ammonium and phosphate by alkaline-activated and lanthanum-impregnated zeolite. *Chemosphere* 164, 387–395. https://doi.org/10.1016/j.chemosphere.2016.08.110 (2016).
- 31. You, K. et al. Lanthanum-modified magnetic oyster shell and its use for enhancing phosphate removal from water. *Colloids Surf. A* 633, 127897. https://doi.org/10.1016/j.colsurfa.2021.127897 (2022).
- 32. Zhong, Z. et al. Phosphate sequestration by magnetic La-impregnated bentonite granules: A combined experimental and DFT study. Sci. Total Environ. 738, 139636. https://doi.org/10.1016/j.scitotenv.2020.139636 (2020).
- 33. Elkhlifi, Z. et al. Lanthanum hydroxide engineered sewage sludge biochar for efficient phosphate elimination: Mechanism interpretation using physical modelling. Sci. Total Environ. 803, 149888. https://doi.org/10.1016/j.scitotenv.2021.149888 (2022).
- 34. Zhang, Y., Pan, B., Shan, C. & Gao, X. Enhanced phosphate removal by nanosized hydrated La (III) oxide confined in cross-linked polystyrene networks. *Environ. Sci. Technol.* **50**, 1447–1454. https://doi.org/10.1021/acs.est.5b04630 (2016).
- 35. Yu, J. et al. Activation of lattice oxygen in LaFe (oxy) hydroxides for efficient phosphorus removal. *Environ. Sci. Technol.* 53, 9073–9080. https://doi.org/10.1021/acs.est.9b01939 (2019).
- 36. Zhi, Y. et al. Emerging lanthanum (III)-containing materials for phosphate removal from water: A review towards future developments. *Environ. Int.* 145, 106115. https://doi.org/10.1016/j.envint.2020.106115 (2020).
- 37. Liu, J., Wan, L., Zhang, L. & Zhou, Q. Effect of pH, ionic strength, and temperature on the phosphate adsorption onto lanthanum-doped activated carbon fiber. *J. Colloid Interface Sci.* 364, 490–496. https://doi.org/10.1016/j.jcis.2011.08.067 (2011).
- 38. Yoon, S.-Y. et al. Kinetic, equilibrium and thermodynamic studies for phosphate adsorption to magnetic iron oxide nanoparticles. *Chem. Eng. J.* 236, 341–347. https://doi.org/10.1016/j.cej.2013.09.053 (2014).
- 39. Li, G. et al. A study on the performance of a recyclable adsorbent La@Fe for phosphate adsorption in wastewater. *Process Saf. Environ. Prot.* 188, 25–38. https://doi.org/10.1016/j.psep.2024.05.075 (2024).
- 40. Fu, H. et al. Superior adsorption of phosphate by ferrihydrite-coated and lanthanum-decorated magnetite. *J. Colloid Interface Sci.* 530, 704–713. https://doi.org/10.1016/j.jcis.2018.07.025 (2018).
- 41. Wang, B. et al. Efficient phosphate elimination from aqueous media by La/Fe bimetallic modified bentonite: Adsorption behavior and inner mechanism. *Chemosphere* 312, 137149. https://doi.org/10.1016/j.chemosphere.2022.137149 (2023).
- 42. Dong, S. et al. Adsorption-electrochemical mediated precipitation for phosphorus recovery from sludge filter wastewater with a lanthanum-modified cellulose sponge filter. Sci. Total Environ. 898, 165545. https://doi.org/10.1016/j.scitotenv.2023.165545 (2023).
- 43. Lan, Y., Gai, S., Cheng, K., Li, J. & Yang, F. Lanthanum carbonate hydroxide/magnetite nanoparticles functionalized porous biochar for phosphate adsorption and recovery: Advanced capacity and mechanisms study. *Environ. Res.* 214, 113783. https://doi.org/10.1016/j.envres.2022.113783 (2022).
- 44. Zhang, F. et al. Sediment phosphorus immobilization with the addition of calcium/aluminum and lanthanum/calcium/aluminum composite materials under wide ranges of pH and redox conditions. *Sci. Total Environ.* 863, 160997. https://doi.org/10.1016/j.scit otenv.2022.160997 (2023).
- 45. Quyen, V. T. et al. Enhanced recovery of phosphate as a value-added product from wastewater by using lanthanum modified carbon-fiber. *Chemosphere* **281**, 130737 (2021).
- 46. Yi, Y., Fu, Y., Wang, Y., Xu, Z. & Diao, Z. Lanthanum/iron co-modified biochar for highly efficient adsorption of low-concentration phosphate from aqueous solution. *J. Environ. Chem. Eng.* 12, 111876. https://doi.org/10.1016/j.jece.2024.111876 (2024).

- 47. Li, M. et al. Different La/Fe oxide composites for efficient phosphate removal from wastewater: Properties and mechanisms. *J. Environ. Chem. Eng.* 10, 107329. https://doi.org/10.1016/j.jece.2022.107329 (2022).
- Ahmed, S. & Lo, I. M. Phosphate removal from river water using a highly efficient magnetically recyclable Fe₃O₄/La (OH)₃ nanocomposite. Chemosphere 261, 128118. https://doi.org/10.1016/j.chemosphere.2020.128118 (2020).
- Shan, S. et al. Remarkable phosphate removal and recovery from wastewater by magnetically recyclable La₂O₂CO₃/γ-Fe₂O₃ nanocomposites. J. Hazard. Mater. 397, 122597. https://doi.org/10.1016/j.jhazmat.2020.122597 (2020).
- 50. Yang, Y. et al. An innovative lanthanum carbonate grafted microfibrous composite for phosphate adsorption in wastewater. J. Hazard. Mater. 392, 121952. https://doi.org/10.1016/j.jhazmat.2019.121952 (2020).
- 51. Yin, H., Zhang, M., Huo, L. & Yang, P. Efficient removal of phosphorus from constructed wetlands using solidified lanthanum/ aluminum amended attapulgite/biochar composite as a novel phosphorus filter. *Sci. Total Environ.* 833, 155233. https://doi.org/10.1016/j.scitotenv.2022.155233 (2022).

Author contributions

Conceptualization, H.L., and H.W.; methodology, Z.J.; software, B.H.; validation, B.H.; formal analysis, H.W.; investigation, T.Q., W.W., and L.C; resources, H.L.; data curation, J.Y.; writing—original draft preparation, H.W.; writing—review and editing, H.L., and J.Y.; visualization, B.H., R.H., and M.L.; supervision, H.L.; project administration, H.L.; funding acquisition, H.L. All authors have read and agreed to the published version of the manuscript.

Funding

This study was supported by the National Natural Science Foundation of China (52108322), Xinjiang Biomass Solid Waste Resources Technology and Engineering Center of China (KSUGCZX2022), Lianyungang Key Research and Development Plan (Social Development) project of China (SF2130), Lianyungang Key Research and Development Plan (Industrial Outlook and Key Technology Core) project of China (CG2207), Postgraduate Research & Practice Innovation Program of Jiangsu Province, grant numbers (SJCX23_1814, SJCX23_1816, and KYCX2023-24), and The Natural Science Foundation of the Jiangsu Higher Education Institutions of China (22KJB560001).

Declarations

Competing interests

The authors declare no competing interests.

Additional information

Correspondence and requests for materials should be addressed to H.L.

Reprints and permissions information is available at www.nature.com/reprints.

Publisher's note Springer Nature remains neutral with regard to jurisdictional claims in published maps and institutional affiliations.

Open Access This article is licensed under a Creative Commons Attribution-NonCommercial-NoDerivatives 4.0 International License, which permits any non-commercial use, sharing, distribution and reproduction in any medium or format, as long as you give appropriate credit to the original author(s) and the source, provide a link to the Creative Commons licence, and indicate if you modified the licensed material. You do not have permission under this licence to share adapted material derived from this article or parts of it. The images or other third party material in this article are included in the article's Creative Commons licence, unless indicated otherwise in a credit line to the material. If material is not included in the article's Creative Commons licence and your intended use is not permitted by statutory regulation or exceeds the permitted use, you will need to obtain permission directly from the copyright holder. To view a copy of this licence, visit https://creativecommons.org/licenses/by-nc-nd/4.0/.

© The Author(s) 2025